magnetochemistry

MDPI

Article

Heptanuclear $[Fe^{III}_6Cr^{III}]^{3+}$ Complexes Experimentally Studied by Means of Magnetometry, X-ray Diffraction, XAS, XMCD and Spin-Polarized Electron Spectroscopy in Cross-Comparison with $[Mn^{III}_6Cr^{III}]^{3+}$ Single-Molecule Magnets

Niklas Dohmeier [1], Andreas Helmstedt [1], Norbert Müller [1], Aaron Gryzia [1], Armin Brechling [1], Ulrich Heinzmann [1,*], Maik Heidemeier [2], Erich Krickemeier [2], Anja Stammler [2], Hartmut Bögge [2], Thorsten Glaser [2], Loïc Joly [3] and Karsten Kuepper [4,†]

1 Faculty of Physics, Bielefeld University, Universitätsstr. 25, 33615 Bielefeld, Germany; niklas.dohmeier@physik.uni-bielefeld.de (N.D.); helmstedt.andreas@gmail.com (A.H.); nmueller@physik.uni-bielefeld.de (N.M.); gryzia@physik.uni-bielefeld.de (A.G.); armin.brechling@uni-bielefeld.de (A.B.)

2 Faculty of Chemistry, Bielefeld University, Universitätsstr. 25, 33615 Bielefeld, Germany; tglaser@uni-bielefeld.de (M.H.); sekretariat-glaser@uni-bielefeld.de (E.K.); anja.stammler@uni-bielefeld.de (A.S.); boegge@uni-bielefeld.de (H.B.); thorsten.glaser@uni-bielefeld.de (T.G.)

3 Institut de Physique et Chimie des Matériaux de Strasbourg, UMR 7504, CNRS-Université de Strasbourg, BP 43, 23 rue du Loess, F-67034 Strasbourg, Cedex 2, France; loic.joly@ipcms.unistra.fr

4 Institut für Festkörperphysik, Universität Ulm, 89069 Ulm, Germany; kkuepper@uni-osnabrueck.de

* Correspondence: uheinzm@physik.uni-bielefeld.de; Tel.: +49-521-106-5469; Fax: +49-521-106-6001

† Current address: Department of Physics, Osnabrück University, Barbarastraße 7, 49076 Osnabrück, Germany.

Academic Editors: Curtis Zaleski and Thaddeus Boron
Received: 9 November 2015; Accepted: 26 January 2016; Published: 5 February 2016

Abstract: Subsequent to the similar $[Mn^{III}_6Cr^{III}]^{3+}$ single-molecule magnets (SMM), the recently studied $[Fe^{III}_6Cr^{III}]^{3+}$ structural type adsorbed thin films prepared on Si and gold-coated glass substrates have been experimentally studied by means of spin-polarized electron spectroscopy (SPES) and X-ray magnetic circular dichroism (XMCD) at the Fe $L_{3,2}$ edge using circularly-polarized synchrotron radiation. The results are cross-compared to the corresponding data obtained from the recently published measurements with Mn-based SMM [1], also in terms of the local spin and orbital magnetic moments obtained. Furthermore, $[Fe^{III}_6Cr^{III}]^{3+}$ single crystals have been experimentally studied by means of magnetometry and X-ray diffraction.

Keywords: single-molecule magnets; molecular magnetism; molecular adsorbates; photoemission; electron spin polarization; XMCD; magnetic moments

1. Introduction

The amount of data produced and stored is increasing rapidly [2]. Whilst the storage of data relies mainly on hard disc drives, the fundamental limitations [3–5] of magnetic recording principles limit recording density to around 1 Tbit/inch^2 [3,6]. Efforts are currently being made involving single molecules performing as memory cells, transistors and even logical devices [7–9], which could replace bulk magnetic and semiconductor devices. A comprehensive review of the subject is given in [10]. Single-molecule magnets (SMM) [11–13] offer a promising approach in terms of

both quantum computing and information storage [14–17]. Single-molecule magnets need to be addressed individually to retrieve stored information; the first successful attempts at depositing SMM on surfaces with preferential orientation [18] and in periodic 2D arrays [19] therefore represent significant developments on the way towards future applications.

It was a "serendipitous approach" [20] that led to the discovery of $Mn_{12}{}^{ac}$, the first single-molecule magnet [21–23]. An alternative method based on rational bottom-up molecular design was found to achieve the $\mathbf{[Mn^{III}{}_6Cr^{III}]^{3+}}$ single-molecule magnet [24–26]. This is representative of the more general $\mathbf{[M^t{}_6M^c]^{n+}}$ structure type, which has been the subject of extensive studies over recent years [24–35].

Earlier studies that investigated the stability of the $\mathbf{[Mn^{III}{}_6Cr^{III}]^{3+}}$ SMM deposited on a variety of substrates against soft X-ray irradiation [36] indicated already the important role in radiation stability played by the anions associated with the SMM core. The initial SMM experiments using spin-resolved electron spectroscopy (SPES) [1,37] were performed using the highly stable $\mathbf{[Mn^{III}{}_6Cr^{III}]^{3+}}$ type with perchlorate anions, and the results were quantitatively cross-compared to XMCD measurements [1]. With controlled deposition of $\mathbf{[Mn^{III}{}_6Cr^{III}]^{3+}}$ SMM arrays on surfaces representing the issue for future applications, the deposition behavior on these surfaces was also studied by non-contact AFM, which revealed 2D-array structures of both commensurate and incommensurate adsorbates [38,39].

The slow relaxation of the magnetization characteristic for single-molecule magnets arises from an energy barrier U^{eff} for spin reversal due to an anisotropy of the spin S_t. This energy barrier U^{eff} was proposed to be equal $D * S_t{}^2$ with S_t being the spin ground state of the whole molecule and D being the zero-field splitting of S_t. [11–13]. The zero-field splitting D describes phenomenologically the anisotropy of the spin, while the physical origin of the anisotropy is due to some orbital angular momentum contribution to the spin [25]. The spin ground state S_t in the heptanuclear complexes $\mathbf{[M^t{}_6M^c]^{n+}}$ arises from the exchange coupling of the local spins S_i of the seven metal ions. The local spin of the Mn^{III} ($S_i = 2$) is known to have a relatively large zero-field splitting. Therefore, it is was chosen for the single-molecule magnet $\mathbf{[Mn^{III}{}_6Cr^{III}]^{3+}}$ [25]. Here, we want to study the effect of substituting the six Mn^{III} ions by six Fe^{III} ions. The Fe^{III} ions have a higher local spin quantum number $S_i = 5/2$, but are less anisotropic and possess a smaller absolute value of the zero-field splitting D. By assuming the same exchange coupling scheme as in $\mathbf{[Mn^{III}{}_6Cr^{III}]^{3+}}$, which has a total spin ground state of $S_t = 21/2$, we expect a higher spin ground state of $S_t = 27/2$ for $\mathbf{[Fe^{III}{}_6Cr^{III}]^{3+}}$. It is an advantage of our systems that we can synthesize the same molecular structure $\mathbf{[M^t{}_6M^c]^{n+}}$ with different metal ions. Thus, we can investigate in an isostructural series the influence of S_i and D on the energy barrier U^{eff} and, hence, the magnetic properties.

The work here involved performing SPES measurements at the $L_{3,2}$ edge of the Fe ions of the comparable $\mathbf{[Fe^{III}{}_6Cr^{III}]^{3+}}$ perchlorate adlayer system by means of circularly-polarized synchrotron radiation. XMCD measurements were also carried out in order to allow a cross-comparison with the electron spin polarization spectra. It is the scope of this article to present the experimental results of spin-resolved electron spectroscopy, as well as of XMCD on $\mathbf{[Fe^{III}{}_6Cr^{III}]^{3+}}$ thin films for the first time and also to cross-compare these with the corresponding $\mathbf{[Mn^{III}{}_6Cr^{III}]^{3+}}$ SMM results in terms of local spin and orbital magnetic moments obtained.

2. Scientific Background

The key factor in the XMCD method becoming a versatile, widely-used tool for investigating the magnetic properties of solids was the availability of high-quality synchrotron radiation sources that could provide variable polarization [40–42]. For this technique, however, it is necessary for the samples to exhibit magnetic orientation, a precondition commonly achieved using strong external magnetic fields together with very low sample temperatures.

The XMCD method owes its broad practical applicability to the discovery of the so-called sum rules regarding the orbital [43] and the spin magnetic moment [44], which relate the measured helicity-dependent absorption difference to the local orbital and spin magnetic moments of the absorbing atom [45,46] element specifically. The accuracy of the derived spin and orbital magnetic

moments is however limited by the approximations used for obtaining the sum rules; see [47–51]. In the case of 3d transition metal ions in particular, corrections to the spin sum rule results must be made, either by using correction factors [52] or comparing the XMCD data to the results from multiplet calculations [53] as used for the **[Mn$^{III}_6$Cr^{III}]$^{3+}$** SMM [1,54]. Applying external magnetic fields in the XMCD experiment constitutes an influence on the investigated systems, which has the potential of changing the sample properties with regard to the undisturbed state without such external fields.

Experiments on paramagnetic Gd in 2001 [55] already indicated that the spin-resolved electron spectroscopy of the samples in the paramagnetic regime beyond the Curie temperature produces the same information as XMCD data, but without having to apply external magnetic fields: The primary excitation step using circularly-polarized radiation is regulated by the relativistic dipole selection rules for both paramagnetic samples and magnetically-oriented materials [56,57]. In both cases, the excitation leads to the generation of oriented core holes in the sample. The core hole orientation resulting from this primary excitation can be investigated by analysis of the spin polarization of Auger electrons subsequent to the decay of the primary core hole. Following the results recently obtained with **[Mn$^{III}_6$Cr^{III}]$^{3+}$** SMM [1], the orientation of the primary core holes was retrieved for the results presented here using the LMV Auger decay (LM: inner shell quantum numbers; V: valence band) of the Fe constituents in the **[Fe$^{III}_6$Cr^{III}]$^{3+}$** system.

XMCD experiments using circularly-polarized light lead to two varying absorption yields [44] Y_+ and Y_- depending on whether the light helicity (the photon angular momentum) is parallel or antiparallel with regard to the preferential magnetic direction (**M**) present in the sample. Whilst **M** is defined by the magnetization in magnetically-ordered solids, an external magnetic field of adequate strength **B** is needed to define **M** in the case of assemblies of non-interacting localized magnetic moments, for example for SMM. As the spin orientation of a magnetized sample runs antiparallel to **M**, the presence of empty 3d valence states results in $Y_+ > Y_-$ for the L_3 edge of the 3d transition metal investigated here. There is a close link between the resulting XMCD asymmetry $A_{XMCD} = (Y_+ - Y_-)/(Y_+ + Y_-)$ and the core hole orientation created by excitation with circularly-polarized radiation in a magnetically non-ordered sample. This close relationship between MCD effects during photoexcitation and the spin polarization of electrons that are emitted from paramagnetic samples has already been described within the framework of the electric dipole approximation; see [58]. The equivalency of both of these approaches is limited to situations in the MCD experiment in which there is no spectroscopic resolution of the exchange splitting [59]. Furthermore, consideration must be given to core level splitting and other effects induced by the core-valence interaction in magnetic samples [60]. In the case of a pure singlet coupling of the Auger decay, an opposite sign of the XMCD asymmetry and of the Auger electron spin polarization is expected [1,59].

3. Experimental Approach

3.1. [{(talen$^{t-Bu_2}$)(Fe^{III}(MeOH))$_3$}$_2${Cr^{III}(CN)$_6$}](ClO$_4$)$_3$ ([Fe$^{III}_6$Cr^{III}](ClO$_4$)$_3$)

A solution of $Fe(ClO_4)_3 \cdot 10H_2O$ (73 mg, 0.14 mmol) in MeOH (10 mL) was heated to a suspension of H_6talen$^{t-Bu_2}$ (50 mg, 0.045 mmol) in MeOH (40 mL). To the brown solution was added a solution of NEt_3 (26 mg, 0.27 mmol) in MeOH (2 mL) and a solution of $K_3[Cr(CN)_6]$ (15 mg, 0.045 mmol) in H_2O (1 mL). The resulting blue solution was stirred for 16 h at room temperature and filtered. Slow evaporation of the filtrate afforded blue-black crystals. Yield: 15 mg (18%). ESI-MS (MeOH): *m*/*z*: 918.1 [{(talen$^{t-Bu_2}$)Fe$_3$}$_2${Cr(CN)$_6$}]$^{3+}$; MALDI-TOF-MS (matrix DCTB): *m*/*z*: 2951 [{(talen$^{t-Bu_2}$)Mn$_3$}$_2${Cr(CN)$_6$}(ClO$_4$)$_2$]$^+$, 2851 [{(talen$^{t-Bu_2}$)Mn$_3$}$_2${Cr(CN)$_6$}(ClO$_4$)]$^+$, 2751 [{(talen$^{t-Bu_2}$)Mn$_3$}$_2${Cr(CN)$_6$}]$^+$; IR (KBr): $\tilde{\nu}$ (cm^{-1}) = 2954 m, 2906 m, 2867 m, 2166 w, 1616 s, 1578 s, 1538 m, 1496 vs, 1435 m, 1393 m, 1364 m, 1339 w, 1312 w, 1258 s, 1190 w, 1140 m, 1111 m, 846 m, 623 w, 563 w, 548 w (Note: vs, s, m, w, means very strong, strong, medium, weak).

Elemental analysis (%): calcd. for [{(talen$^{t-Bu_2}$)(Fe^{III}(MeOH))$_3$}$_2${Cr^{III}(CN)$_6$}](ClO_4)$_3$· 9H_2O· $KClO_4$ ($C_{150}H_{234}N_{18}O_{43}KCl_4CrFe_6$): C 50.81, H 6.65, N 7.11; found: C 50.51, H 6.31, N 7.10.

3.2. X-ray Crystallography

[$Fe^{III}_6Cr^{III}$](BPh_4)$_3$· 12MeOH· 2H_2O, $C_{234}H_{328}N_{18}O_{32}B_3CrFe_6$, M = 4324.67, monoclinic, space group $P2_1/n$ (No. 14), a = 21.8535(9), b = 17.8316(8), c = 31.2963(13) Å, β = 90.641(2), V = 12194.9(9) Å^3, Z = 2, T = 100(2) K, μ(MoKα) = 0.456 mm^{-1}, ρ_{calc} = 1.178 g/cm^3, crystal size = 0.254 × 0.196 × 0.14 mm^3, 179,177 reflections measured ($3.94 \leqslant 2\Theta \leqslant 50.00^\circ$), 21,425 unique reflections used in the refinements (R_{int} = 0.0438). The final R_1 values (1261 refined parameters) were 0.0644 for 16,427 reflections with $I > 2\sigma(I)$ and 0.0810 for all data.

Single crystals of **[$Fe^{III}_6Cr^{III}$]**(BPh_4)$_3$· 12MeOH· 2H_2O were removed from the mother liquor, coated with oil and immediately cooled to 100(2) K on a Bruker (Madison, WI, USA) Kappa-APEX-II four-circle diffractometer with a 4K CCD detector, MoKα radiation, graphite monochromator. SADABS-2008/1 (Bruker AXS Inc., Madison, WI, USA) was used for absorption correction; solution and refinement were done with SHELXS/L [61]. At early stages of refinement, 6 MeOH and 1 H_2O molecules were found in the asymmetric unit, but could not properly be refined and were therefore removed from the coordinate set. The resulting void was then examined with "SQUEEZE" [62]. The found electron count can be attributed to approx. 6 MeOH molecules and 1 H_2O molecule. These were included in the given sum formula and, thus, contribute to the derived quantities, like μ, *etc.*

CCDC-1419972 contains the supplementary crystallographic data for this paper. These data can be obtained free of charge from [63].

3.3. Other Physical Measurements

Infrared spectra (400–4000 cm^{-1}) of solid samples were recorded on a Shimadzu (Kyoto, Japan) FT-IR 8400S as KBr disks. ESI and MALDI-TOF mass spectra were recorded on a Bruker (Billerica, MA, USA) Esquire 3000 ion trap mass spectrometer or a Waters QUATTRO LCZ mass spectrometer and a PE Biosystems Voyager (Weiterstadt, Germany) DE mass spectrometer or a Bruker (Billerica, MA, USA) REFLEX IV mass spectrometer, respectively. Elemental analyses were carried out on a LECO (St. Joseph, MI, USA) CHN-932 or a HEKAtech Euro (Wegberg, Germany) EA elemental analyzer. ^{57}Fe Mössbauer spectra were recorded on an alternating constant-acceleration spectrometer. The sample temperature was maintained constant in a bath cryostat (Wissel (Starnberg, Germany) MBBC-HE0106). ^{57}Co/Rh was used as the radiation source. Isomer shifts were determined relative to α-iron at room temperature. UV/VIS/NIR absorption spectra of solutions were measured on a Shimadzu (Kyoto, Japan) UV-3101PC spectrophotometer in the range 190–1100 nm at ambient temperature. Temperature-dependent magnetic susceptibilities were measured using a SQUID magnetometer (MPMS XL-7 EC, Quantum Design (San Diego, CA, USA)) in a static field of 1 T in the range 2–290 K. Variable-temperature variable-field (VTVH) measurements were performed at various static fields in the range 2–10 K with the magnetization equidistantly sampled on a $1/T$ temperature scale. For calculations of the molar magnetic susceptibilities, χ_m, the measured susceptibilities were corrected for the underlying diamagnetism of the sample holder and the sample by using tabulated Pascal's constants. AC susceptibilities were measured in the range 1.8–5.0 K in zero static field with an AC field of 3 Oe oscillating at frequencies in the range 660–1500 Hz.

3.4. Sample Preparation

Based on our results of Mn-based SMM [1], the **[$Fe^{III}_6Cr^{III}$]**(ClO_4)$_3$ system with perchlorate anions was chosen for the spin-resolved electron spectroscopy and XMCD measurements. Methanolic solutions with a concentration of 6 × 10^{-5} mol/L were prepared.

An airbrush process using an airbrush gun (Grafo T1 by Harder & Steenbeck GmbH & Co. KG, Norderstedt, Germany) and using high purity nitrogen (99.999%) as the working gas at a pressure of 1.25 bar was used for the **[$Fe^{III}_6Cr^{III}$]$^{3+}$** sample preparation: a square substrate with an edge length of

approximately 11 mm was coated with 200 µL of methanolic solution, through repeatedly moving the airbrush nozzle across the substrate.

The described method allowed the deposition of homogeneous adsorbate deposits with an area of up to 100 mm^2 at a distance of 40 mm with respect to the nozzle of 0.15 mm in diameter. Si(110) and gold-coated glass substrates (Arrandee by Dr. Dirk Schröer, Werther, Germany) were used for this work. It should be noted that the airbrush deposition method leads to a macroscopic $\mathbf{[Fe_6Cr]^{3+}}$ deposit on the substrate surface. Optical microscopy proves that the deposited layer can be regarded as homogeneous on the size scale of the synchrotron radiation spot size of approximately 1 mm^2. The structure of the layer with a thickness of about 10 µm as seen by optical microscopy given in Figure 1 appears similar to the structure observed for $\mathbf{[Mn^{III}_6Cr^{III}]^{3+}}$ SMM deposited by the same preparation step; see Figure 1 of [1]. Thus, the results presented here represent $\mathbf{[Fe_6Cr]^{3+}}$ polycrystalline bulk measurements.

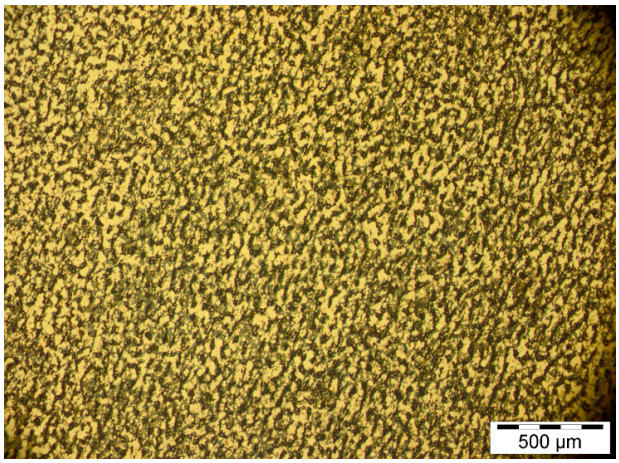

Figure 1. Optical microscopy image of the $\mathbf{[Fe^{III}_6Cr^{III}]}(ClO_4)_3$ thin film. The synchrotron X-ray radiation spot of about a 1-mm^2 size averaged over the polycrystalline cluster structure of the film.

4. Results and Discussion

4.1. Synthesis and Characterization of $[Fe^{III}_6Cr]^{3+}$

The heptanuclear complexes $\mathbf{[M^t_6M^c]^{n+}}$ (=$[\{(talen^{tBu_2})M^t_3\}_2\{M^c(CN)_6\}]^{n+}$) using the triplesalen ligand $H_6talen^{t-Bu_2}$ (Scheme 1) have yet only been prepared with the terminal ions $M^t = Mn^{III}$ [24,26,27,29–33,35].

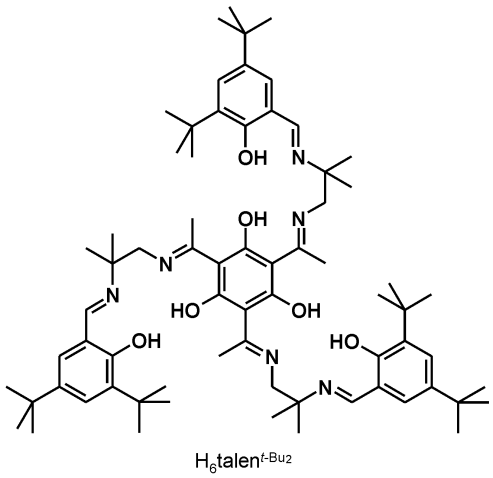

Scheme 1. Triplesalen used for the synthesis of the complex.

However, trinuclear complexes with Fe^{III} ions coordinated by the triplesalen ligand were obtained [30,64]. Moreover, using the related chiral triplesalen ligand H_6chand^{RR}, the heptanuclear complex $^{RR}[Fe^{III}{}_6Fe^{II}]^{2+}$ was synthesized and characterized [34]. In analogy to these reactions in order to obtain $\mathbf{[Fe^{III}{}_6Cr^{III}]^{3+}}$, we have reacted $H_6talen^{t-Bu_2}$ with $Fe^{III}(ClO_4)_3 \cdot 10H_2O$, resulting in a blue solution typical for phenolate-to-Fe^{III} LMCT (ligant-to-metal charge transfer) absorptions. Addition of $K_3[Cr^{III}(CN)_6]$ provided blue crystals of $\mathbf{[Fe^{III}{}_6Cr^{III}]}(ClO_4)_3$ as evidenced by the ν(C≡N) = 2166 cm^{-1} stretching mode and the observation of $\mathbf{[Fe^{III}{}_6Cr^{III}]^{3+}}$ in the mass spectra. The UV-VIS spectrum (Figure 2) exhibits, besides the strong absorptions of the heteroradialene backbone between 27,000 and 35,000 cm^{-1}, the prominent phenolate-to-Fe^{III} LMCT transition at 18,300 cm^{-1}. This is lower in energy than the phenolate-to-Mn^{III} LMCT in $\mathbf{[Mn^{III}{}_6Cr^{III}]^{3+}}$ at ~23,000 cm^{-1} due to the lower effective nuclear charge of Mn^{III}.

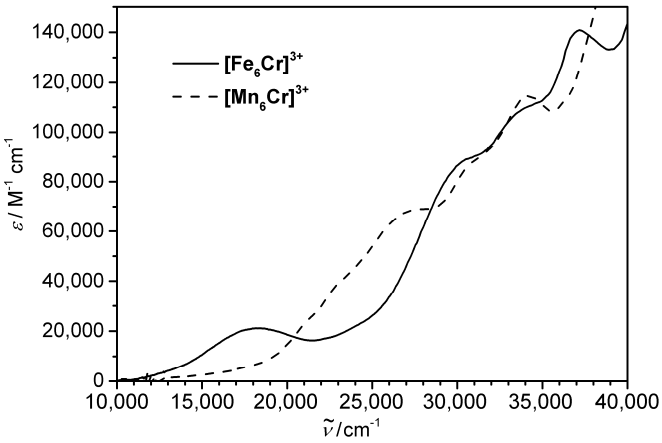

Figure 2. Electronic absorption spectra of $\mathbf{[Fe^{III}{}_6Cr^{III}]}(ClO_4)_3$ and $\mathbf{[Mn^{III}{}_6Cr^{III}]}(BPh_4)_3$ measured in MeCN.

Single-crystal X-ray diffraction on $\mathbf{[Fe^{III}{}_6Cr^{III}]}(ClO_4)_3$ proved the formation of the heptanuclear complex $\mathbf{[Fe^{III}{}_6Cr^{III}]^{3+}}$. Interestingly, this compound crystallizes in the cubic space group $I\bar{a}3$ with the crystallographically imposed C_3 axes forming the space diagonals of the cubic unit cell. However, the quality of the diffraction data did not allow refining the structure sufficiently (R = 12.12%). In our work on $\mathbf{[M^t{}_6M^c]^{n+}}$, we recognized that the quality of the single crystals for single-crystal X-ray diffraction could be enhanced by using BPh_4^- as the counter ion [26]. Therefore, we added $NaBPh_4$ to the reaction mixture and obtained after recrystallization from MeOH bluish-black crystals, which were analyzed by single-crystal X-ray diffraction as $\mathbf{[Fe^{III}{}_6Cr^{III}]}(BPh_4)_3 \cdot 12MeOH \cdot 2H_2O$. The molecular structure of the heptanuclear complex $\mathbf{[Fe^{III}{}_6Cr^{III}]^{3+}}$ constitutes two trinuclear $[(talen^{t-Bu_2})Fe^{III}\}]^{3+}$ units connected by a central $[Cr^{III}(CN)_6\}^{3-}$ (Figure 3a). The asymmetric unit consists of only half of the heptanuclear complex (Figure 3b); the other half is generated by a crystallographic center of inversion. All Fe^{III} ions are six-coordinated by the additional coordination of a MeOH solvent molecule.

Selected interatomic distances are provided in Table 1. The Mn^{III} ions in $\mathbf{[Mn^{III}{}_6Cr^{III}]^{3+}}$ are Jahn–Teller active, *i.e.*, the coordinated sphere can be described as a tetragonally-elongated octahedron with the N_2O_2 environment of the salen-like coordination compartments forming the basal plane. The cyanides coordinate in the Jahn–Teller axes, while the positions trans to the cyanides are either occupied by solvent molecules or empty. The Fe^{III} in $\mathbf{[Fe^{III}{}_6Cr^{III}]^{3+}}$ is not Jahn–Teller active. This has two main consequences: the Fe^{III} ions are all six-coordinated, and the Fe–$N^{N\equiv C}$ bonds are shorter (2.10 Å) than the Mn–$N^{N\equiv C}$ bonds (2.17–2.22 Å) in $\mathbf{[Mn^{III}{}_6Cr^{III}]^{3+}}$ [26]. A further notable difference in the molecular structure of $\mathbf{[Fe^{III}{}_6Cr^{III}]^{3+}}$ to that of $\mathbf{[Mn^{III}{}_6Cr^{III}]^{3+}}$ is a lower heteroradialene character of the central six-membered ring, which is evidenced by a HOMA value (harmonic oscillator model of aromaticity) [65,66] of 0.81 for $\mathbf{[Fe^{III}{}_6Cr^{III}]^{3+}}$, while values of 0.6–0.7 are indicative of a stronger heteroradialene character in $\mathbf{[Mn^{III}{}_6Cr^{III}]^{3+}}$.

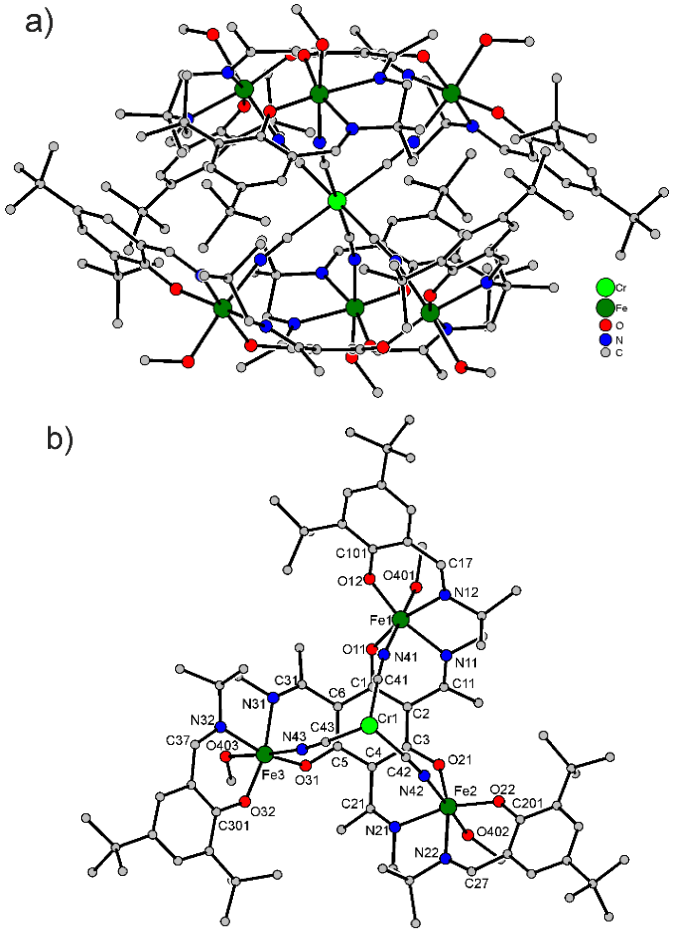

Figure 3. (**a**) Molecular structure of $[Fe^{III}_6Cr^{III}]^{3+}$ in single crystals of $[Fe^{III}_6Cr^{III}](BPh_4)_3 \cdot 12MeOH \cdot 2H_2O$; (**b**) asymmetric unit of $[Fe^{III}_6Cr^{III}]^{3+}$ and the numbering scheme used. Hydrogen atoms have been omitted for clarity.

Table 1. Selected interatomic distances (Å) in $[Fe^{III}_6Cr^{III}]^{3+}$.

Fe1–O11	1.902(2)	O32–C301	1.325(4)
Fe1–O12	1.888(2)	N11–C11	1.291(4)
Fe1–N11	2.110(3)	N12–C17	1.298(4)
Fe1–N12	2.104(3)	N21–C21	1.293(4)
Fe1–N41	2.095(3)	N22–C27	1.290(4)
Fe1–O401	2.141(3)	N31–C31	1.293(5)
Fe2–O21	1.908(2)	N32–C37	1.291(5)
Fe2–O22	1.895(2)	N41–C41	1.149(4)
Fe2–N21	2.111(3)	N42–C42	1.147(4)
Fe2–N22	2.101(3)	N43–C43	1.149(4)
Fe2–N42	2.113(3)	C1–C2	1.416(5)
Fe2–O402	2.103(2)	C2–C3	1.422(5)
Fe3–O31	1.907(2)	C3–C4	1.415(5)
Fe3–O32	1.890(2)	C4–C5	1.416(5)
Fe3–N31	2.102(3)	C5–C6	1.410(5)
Fe3–N32	2.101(3)	C6–C1	1.411(5)
Fe3–N43	2.098(3)	C2–C11	1.470(5)
Fe3–O403	2.159(2)	C4–C21	1.482(4)
Cr1–C41	2.060(4)	C6–C31	1.487(5)
Cr1–C43	2.059(3)		
Cr1–C42	2.068(4)	Cr1···Fe1	5.2582(5)
O11–C1	1.333(4)	Cr1···Fe3	5.2602(5)
O21–C3	1.312(4)	Cr1···Fe2	5.2758(5)
O31–C5	1.326(4)	Fe1···Fe3	6.7678(7)
O12–C101	1.322(4)	Fe1···Fe2	6.8200(7)
O22–C201	1.319(4)	Fe2···Fe3	6.7415(7)

The ^{57}Fe Mössbauer spectrum of $[Fe^{III}_6Cr^{III}](ClO_4)_3$ (Figure 4) exhibits a single quadrupole doublet with an isomer shift of 0.51 mm·s^{-1} and quadrupole-splitting of 1.97 mm·s^{-1}, demonstrating the presence of Fe^{III} (d^5, $S_i = 5/2$) ions.

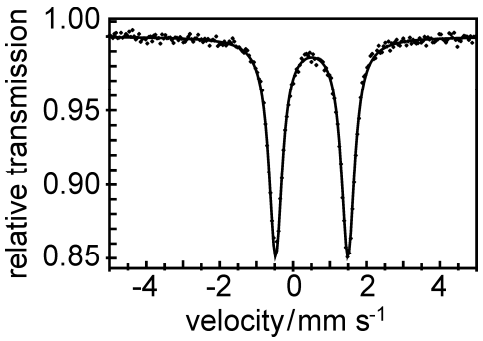

Figure 4. ^{57}Fe Mössbauer spectrum of $[Fe^{III}_6Cr^{III}]^{3+}$ at 80 K. The solid lines correspond to simulations with the parameters provided in the text.

The effective magnetic moment, μ_{eff}, decreases from 14.89 μ_B at 290 K to a minimum of 14.19 μ_B at 20 K and increases to 14.47 μ_B at 8 K and then drops to 14.38 μ_B at 5 K (Figure 5a). The VTVH (variable-field variable-temperature) magnetization measurements (Figure 5b) provide some nesting behavior indicative of some magnetic anisotropy. The low temperature (2 K) high field (7 T) magnetization value is 25.6 μ_B. These magnetic data are consistent with a small antiferromagnetic Fe^{III}-Cr^{III} exchange interaction, responsible for the decrease of μ_{eff} from room temperature to 20 K. The slight increase below 20 K indicates either a very small ferromagnetic Fe^{III}-Fe^{III} interaction or an antiferromagnetic Fe^{III}-Fe^{III} coupling, resulting in an overall ferrimagnetic coupling scheme, as was also observed for $[Mn^{III}_6Cr^{III}]^{3+}$. Either of these two scenarios results in an $S_t = 27/2$ spin ground state. This value is collaborated from the high saturation magnetization value in the VTVH data. Despite this high spin ground state and the small magnetic anisotropy, $[Fe^{III}_6Cr^{III}]^{3+}$ shows no out-of-phase signal in the AC magnetization measurements for frequencies up to 1500 Hz. Thus, there is no indication that $[Fe^{III}_6Cr^{III}]^{3+}$ exhibits a slow relaxation of the magnetization indicative of SMM behavior.

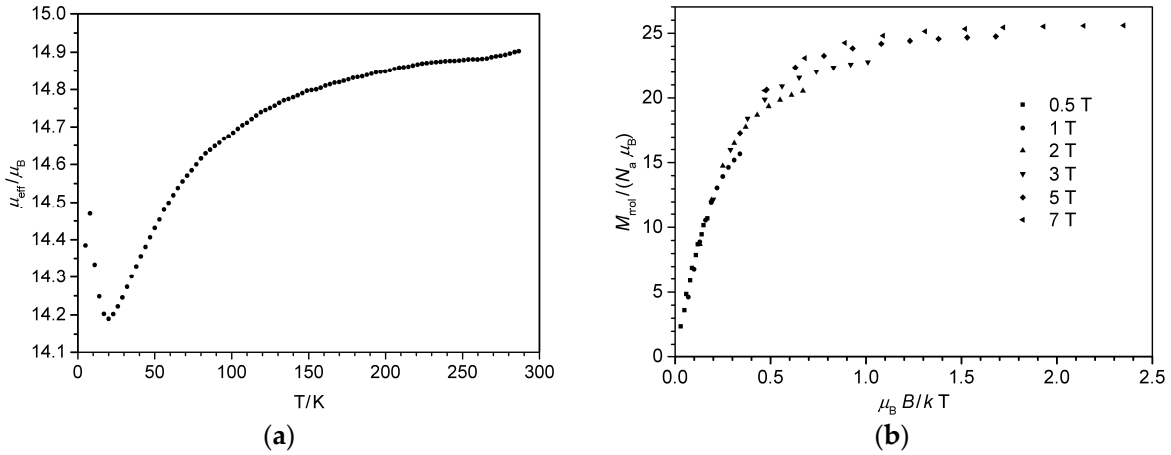

Figure 5. Magnetic measurements of $[Fe^{III}_6Cr^{III}]^{3+}$: (**a**) temperature dependence of μ_{eff} at 1 T; (**b**) variable-field variable-temperature (VTVH) magnetization measurements at the given magnetic fields.

4.2. Radiation Sensitivity

The large homogeneous sample area as described in Section 3.4 allowed a sample scanning during the spin polarization measurements: results obtained from many sample positions are merged into one spin polarization data point, thus overcoming the limitation of the measurement time due to the $\mathbf{[Fe^{III}_6Cr^{III}]^{3+}}$ radiation sensitivity. Both this radiation sensitivity of the $\mathbf{[Fe^{III}_6Cr^{III}]^{3+}}$ molecule and the homogeneity and the condition of the deposited $\mathbf{[Fe^{III}_6Cr^{III}]^{3+}}$ adlayer were measured by means of $L_{3,2}$ edge XAS characterization. This is demonstrated in Figure 6, where a noticeable reduction of the ions in the molecule from Fe^{III} to Fe^{II} for high photon pre-exposure is shown. Therefore, the sample has been scanned in the final measurement to ensure that not more than 3×10^{13} photons hit the irradiated sample, which corresponds to more than 90% Fe^{III} and not more than 10% Fe^{II}.

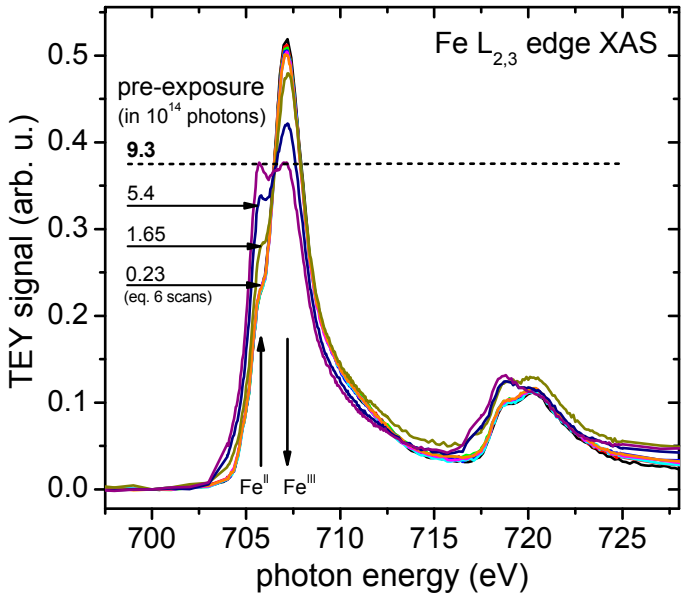

Figure 6. XAS total electron yield (TEY) spectra showing the radiation-induced change of the Fe oxidation state in $\mathbf{[Fe^{III}_6Cr^{III}](ClO_4)_3}$. The initial Fe^{III} content decreases from 0.98 to 0.20 due to the reduction process occurring upon soft X-ray exposure.

4.3. Spin-Resolved Electron Spectroscopy

The BESSY-II storage ring beamlines UE52-SGM and UE56/2-PGM2 of Helmholtz-Zentrum Berlin (HZB) were used to perform the spin-resolved electron spectroscopy (SPES) measurements shown here. Both beamlines provide a range of photon energies extending from 90 eV–1300 eV and cover the 700 eV region of the Fe $L_{3,2}$ edge, using the synchrotron radiation of permanent magnet undulators. For more information on the specifications of both beamlines, see [67–69].

The ultra-high vacuum (UHV) experimental setup shown in Figure 7 as used in these spin-resolved electron spectroscopy experiments was fit with a 90° spherical field electron spectrometer in the geometry of normal incidence and normal emission. Subsequent to the energy analysis, the electrons were collected and transferred to a spherical Mott Rice-type polarimeter [70], using a scattering energy of max. 45 kV. The Mott polarimeter polarization sensitivity (Sherman function) at 25 kV (45 kV) was measured to be $S_{\mathrm{eff}} = -0.17 \pm 0.02$ ($S_{\mathrm{eff}} = -0.23 \pm 0.02$) [1]. Note that in the following figures, the uncertainty regarding the polarization sensitivity as a scale factor is not regarded in the error bars of the spin-polarized electron spectra.

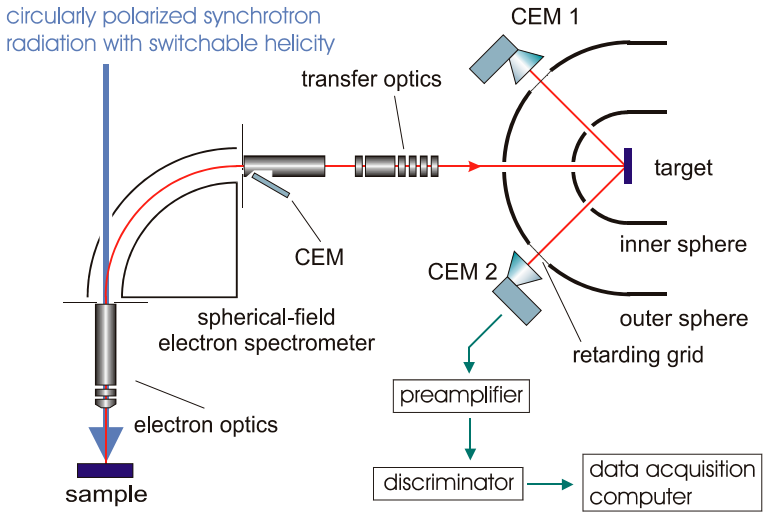

Figure 7. Schematic view of the electron spectrometer and the Mott polarimeter. Also shown is the position of the main electron detectors (**CEM1**, **CEM2**) and the auxiliary detector (**CEM**) mounted off-axis behind a separate exit slit. The Mott polarimeter is shown rotated around its axis by 90°.

The scattered and retarded electrons were detected by channel electron multipliers (CEM by Dr. Sjuts Optotechnik, Göttingen, Germany) with a circular entry funnel (25 mm in diameter) to maximize detection efficiency. The electron spectrometer, as well as the Mott polarimeter have been successfully used before [1,37,55,57,71,72], as has been described in more detail elsewhere; see [57,72]. The UHV setup used an electrically-isolated sample stage for the total electron yield (TEY) mode XAS measurements, a sample transfer and preparation system with UHV storage of up to six samples and a load-lock with a pump-down time of less than 1 h, which allowed frequent sample changes necessary for the limited sample lifetime at soft X-ray exposure [36]. Figure 8 shows Auger and photoelectron spectra of the previously radiation-unexposed **[Fe$^{III}_6$Cr^{III}]**$(ClO_4)_3$ adlayer system measured at 708.0 eV (top data, black) and at 706.6 eV (bottom data, red) photon energies; see also Figure 6.

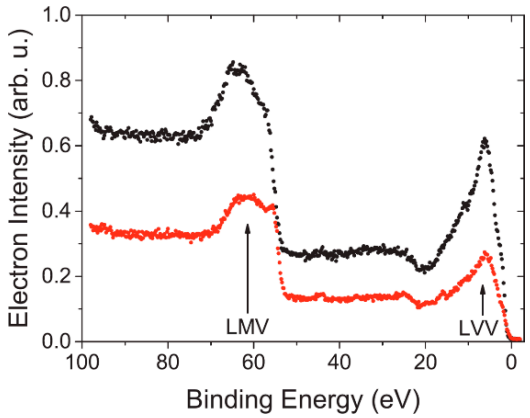

Figure 8. XPS photoelectron and Auger electron spectrum of fresh **[Fe$^{III}_6$Cr^{III}]**$(ClO_4)_3$ thin films for excitation X-ray energies 708.0 eV (top black data points) and 706.6 eV (bottom red data points) as a function of the electron binding energy.

4.4. XMCD Measurements

Comparative XMCD investigations of **[Fe$^{III}_6$Cr^{III}]**$(ClO_4)_3$ thin films have been performed at the X11MA/SIM beamline of the Swiss Light Source (SLS) storage ring at the Paul Scherrer Institute in Villigen, Switzerland. The beamline is based on a double undulator comparable to the UE56

undulators in Berlin at the BESSY-II storage ring. Both undulators are tilted against each other. They can be operated with opposite helicity, which has been used in the present experiment. The XMCD data presented here are obtained at the low temperature T = 4 K and a magnetic field of B = 6.9 T. It has to be noted that the sum rule evaluation as discussed in Section 4.6 requires a sample magnetization up to saturation. This has been fulfilled as the VTVH results in Figure 5 show. All XMCD measurements were done in TEY mode by measuring the sample current; the corresponding yields at the Fe L_{23} edges for the use of circularly-polarized radiation of both helicities and their XMCD difference are shown in Figure 9.

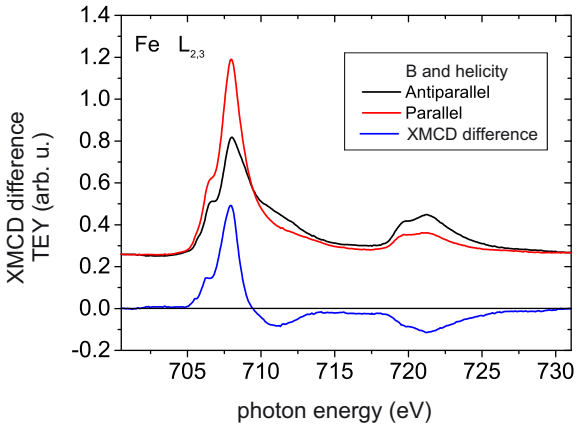

Figure 9. Fe $L_{3,2}$ edge XMCD data obtained from $[Fe^{III}_6Cr^{III}](ClO_4)_3$ at B = 6.9 T and T = 4 K. The helicity-dependent absorption spectra are shown together with the resulting XMCD difference.

4.5. Electron Spin Polarization and XMCD Results of $[Fe^{III}_6Cr^{III}](ClO_4)_3$ Adlayers in the Cross-Comparison with the Corresponding Results of $[Mn^{III}_6Cr^{III}]^{3+}$ SMM

A sample scanning method was used on account for the radiation sensitivity of the molecules (see Figure 6), which involved selecting new and previously unexposed sample positions after each measurement of approximately 60 s in duration. A large number of these measurements were then combined to form a single spin polarization data point. Variations in the adsorbate layer thickness were equalized out, since an evaluation was made only of the asymmetry of the count rates of both detectors. Any asymmetries relating to the CEM detector's differences were cancelled out through combining the measurements with both helicities of the circularly-polarized light used in the excitation process.

Spin polarization results obtained from $[Fe^{III}_6Cr^{III}](ClO_4)_3$ samples at room temperature and without any magnetic field are shown in Figure 10. The result of a comparative XMCD asymmetry study at B = 6.9 T and T = 4 K is represented by the solid line of the top panel. The lower panel of the figure again shows the corresponding absorption spectrum. For $[Fe^{III}_6Cr^{III}](ClO_4)_3$, a negative spin polarization with absolute values up to 25% is predominant in the Fe L_3 edge region.

Figure 11 shows the corresponding results of SPES and XMCD asymmetry for $[Mn^{III}_6Cr^{III}]^{3+}$ SMM [1] in the cross-comparison. While in both systems the energy dependences of spin polarization are almost the same and also agree with respect to the cross-comparison of SPES and XMCD, there is one important difference between both systems in Figures 10 and 11. The spin polarization scale (left part of Figure 10) for the Fe-system is twice the absolute spin polarization scale for the Mn-based system (left part of Figure 11); or in other words, in contrast to the Mn SMM, the absolute value of electron spin polarization measured at room temperature without any external magnetic field quantitatively agrees with the absolute value of the XMCD asymmetry measured a 4 K temperature and a 6.9 T magnetic field for $[Fe^{III}_6Cr^{III}](ClO_4)_3$. This expected behavior [55,59] demonstrates that the corresponding LMV Auger transition in the Fe-based molecular system fulfills much better the

requirement of a pure singlet coupling than took place in the $[Mn^{III}_6Cr^{III}]^{3+}$ SMM-based system; see Figure 11.

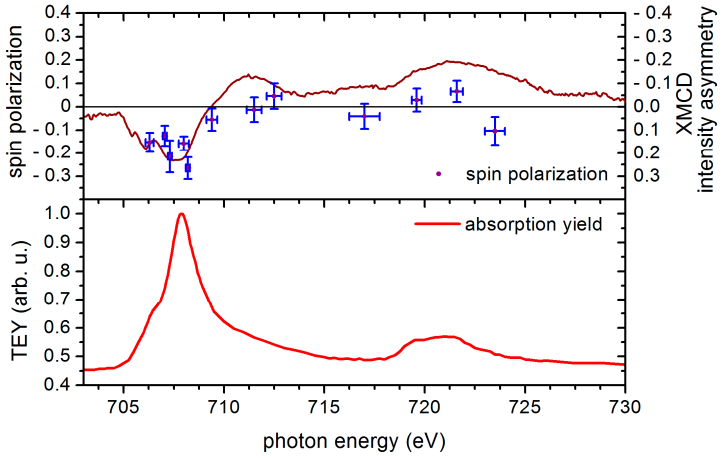

Figure 10. Top panel: The spin polarization of Auger electrons resulting from the LMV $[Fe^{III}_6Cr^{III}]^{3+}$ Auger transition is shown. The horizontal error bars represent the bandwidth of the circularly-polarized radiation used in the excitation step. The vertical error bars correspond to the single statistical error of the measurements. The solid line represents XMCD asymmetry data (6.9 T, 4 K) for the comparison. Bottom panel: A corresponding Fe L-edge absorption spectrum of $[Fe^{III}_6Cr^{III}](ClO_4)_3$ is shown.

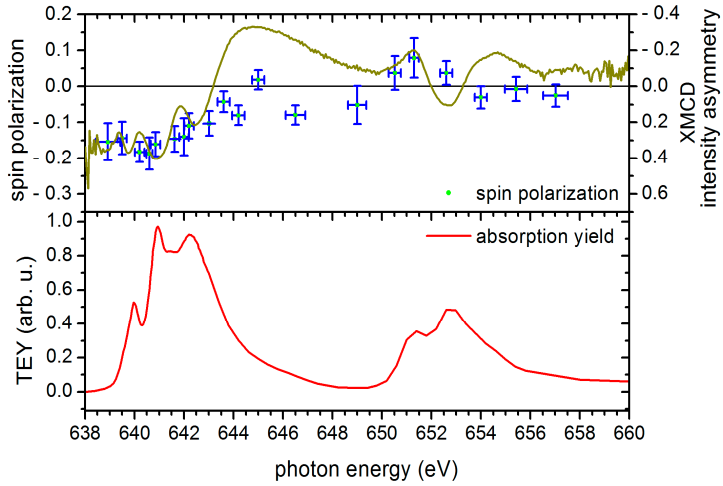

Figure 11. Top panel: Spin polarization and XMCD results obtained from $[Mn^{III}_6Cr^{III}](ClO_4)_3$ single-molecule magnets (SMM) similarly to Figure 10. Bottom panel: Mn $L_{3,2}$ edge absorption spectrum of $[Mn^{III}_6Cr^{III}](ClO_4)_3$ from [1].

Considering that we know that the $[Mn^{III}_6Cr^{III}]^{3+}$ complex is indeed a single-molecule magnet at low temperatures and the $[Fe^{III}_6Cr^{III}]^{3+}$ complex is not, the results of higher electron spin polarization degree measured for the Fe-system than for the Mn SMM are an interesting and perhaps surprising observation.

4.6. Sum Rule Evaluation of SPES and XMCD Data

On the basis of the approach described under scientific background, it should be possible to obtain information from the SPES measurement equivalent to that of the XMCD data. A spin sum rule analysis was therefore undertaken for both methods (see [43–46]).

The spin sum rule approach cannot be universally applied to 3d systems; see [53] for a detailed discussion on the limitations imposed by physical constraints. Since both experimental methods are affected by these constraints in the same way, the sum rule approach still provides a useful tool for cross-comparing XMCD and spin-resolved electron spectroscopy data, as successfully shown already for the $\mathbf{[Mn^{III}_6Cr^{III}]^{3+}}$ SMM [1]. The analysis was therefore performed in the same way for the Fe-system.

The linearly-interpolated SPES data and the corresponding (*i.e.*, doubled) absorption yield measured without an external magnetic field were multiplied pointwise. This multiplication result corresponds to the difference of the two partial intensities $I^{\uparrow}$ and $I^{\downarrow}$, generally being necessary to formulate the XMCD sum rules. $\uparrow$ and $\downarrow$ correspond to spin parallel and antiparallel to the radiation helicity, respectively.

The measurement uncertainty of the spin polarization results shown in Figures 10 and 11 represents the statistical error of the spin polarization measurement due to the electron counting process. It contributes to the uncertainty of the sum rule results by introducing errors in the p and q integrals on which the sum rule evaluation is based. These errors cannot be derived mathematically due to the integration steps being part of the sum rule formalism. The following numerical approach was chosen to derive the uncertainty of the sum rule results from the spin polarization uncertainty: Each spin polarization data point was varied within its error range, assuming a normal distribution of the possible results within this range. For each spin polarization dataset obtained from this variation, the p and q integrals were evaluated as given in Figure 12, and the sum rule results for the spin and orbital magnetic moments were derived. After generating a sufficient number of varied spin polarization datasets (10,000 runs), the standard deviation of the resulting spin and orbital moments was calculated to obtain the uncertainty of the final results.

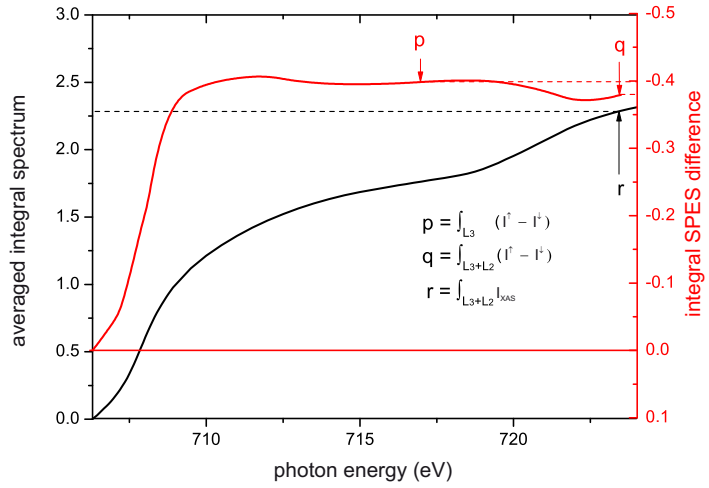

Figure 12. Integration of the product of measured spin polarization linearly interpolated and a doubled averaged XAS intensity spectrum, which corresponds to the difference of partial electron intensities with spin $\uparrow$ and $\downarrow$ and integration of the averaged XAS spectrum obtained from the $\mathbf{[Fe^{III}_6Cr^{III}]}(ClO_4)_3$ thin film yielding the parameters p, q and r needed for the sum rule analysis.

The difficulties posed in fully separating the L_2 and L_3 contributions in 3d systems are widely known: by applying the sum rule expression most commonly used [45,46] and calculating the necessary integrals p (L_3 edge intensity difference), then q ($L_{3,2}$ edge intensity difference) and finally r ($L_{3,2}$ edge helicity averaged absorption), the SPES data for the Fe^{III} ions delivered the following results:

$$\begin{aligned} \mu_{spin} &= \frac{(3p-2q)\,(10-n_{3d})}{r\,k_{corr}} &= 1.4 \pm 0.5\,\mu_{Bohr} \\ \mu_{orbit} &= \frac{2q\,(10-n_{3d})}{3r} &= 0.56 \pm 0.13\,\mu_{Bohr} \end{aligned} \quad (1)$$

In Equation (1), we used the p and q values of Figure 12 with opposite sign because of the opposite sign of XMCD asymmetry and spin polarization due to the singlet Auger decay [1,37]. Since the literature sometimes overlooks the sign differences between σ^+/σ^- light helicities and right/left circular polarization, between electron spin and magnetic moment and finally between different XMCD asymmetry definitions, we follow here the sign convention for the local magnetic moments as done by [46]: a positive local magnetic spin moment means that the spin of the 3d majority electrons is antiparallel to the B field.

It has to be noted that although the contribution of the magnetic dipole Term $\mathbf{<T_z>}$ is supposed to be small for 3d transition metals [52], it cannot always be neglected and plays a significant role in systems of higher symmetry than O_h or low dimensionality, such as thin films or interfaces [73,74]. However, the $\mathbf{<T_z>}$ contribution can be eliminated by averaging measurements in three orthogonal directions, leading to a simplified spin sum rule expression, as described in [74]. The effect of averaging over different directions is the same for situations where the averaging is the result of a polycrystalline sample [74]. The investigations presented within this work were carried out on macroscopic, polycrystalline $\mathbf{[Fe_6Cr]^{3+}}$ deposits on a size scale of about 10 µm; therefore, the $\mathbf{<T_z>}$ contribution was neglected in the sum rule evaluation. On the other hand, a correction factor $\mathbf{k}_{corr}$ was added to the result, in accordance with the suggested approach [53]. For the Fe^{III} system, a correction factor 1.48 was used as given and proposed [52]. It is worth noting that these local spin and orbital magnetic moments agree well with the corresponding values 1.8 ± 0.4 μ_{Bohr} and 0.60 ± 0.12 μ_{Bohr} measured for the Mn^{III} ions in the $\mathbf{[Mn^{III}_6Cr^{III}]^{3+}}$ SMM within the experimental errors given, respectively.

Local spin and orbital magnetic moment results for the Fe^{III} ions were obtained accordingly from the XMCD data shown in Figure 9 via the r, p, q determination given in Figure 13. Once again, the same correction factor was applied to the spin magnetic moment, and the contribution by the magnetic dipole was neglected:

$$\begin{aligned} \mu_{spin} &= \frac{(3p-2q)\,(10-n_{3d})}{r\,k_{corr}} &&= 1.9 \pm 0.3\,\mu_{Bohr} \\ \mu_{orbit} &= \frac{2q\,(10-n_{3d})}{3r} &&= 0.01 \pm 0.03\,\mu_{Bohr} \end{aligned} \tag{2}$$

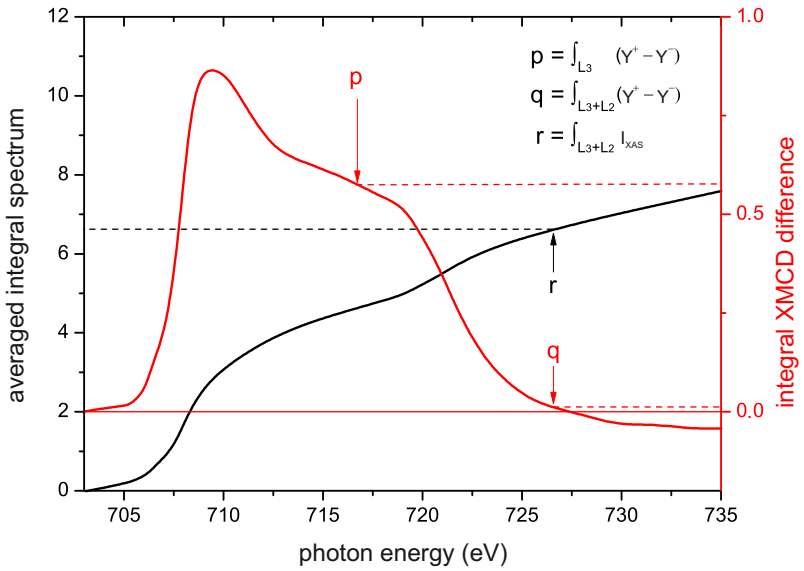

Figure 13. Integration of the XMCD difference signal and of an averaged XAS spectrum obtained from the $\mathbf{[Fe^{III}_6Cr^{III}]}(ClO_4)_3$ thin film yielding the parameters p, q and r needed for the sum rule analysis.

The algorithm that was used to derive the uncertainty of the spin and orbital moments from the spin polarization error was also used for the XMCD evaluation: The XMCD results presented in Figure 9 were obtained by averaging a sufficient number of absorption spectra to reduce noise. The standard deviation associated with each XMCD data point was then used as the input for the variation algorithm described above, leading to an estimate for the total uncertainty of the sum rule results for the spin and orbital magnetic moments. As already mentioned, the necessary complete saturation of the sample magnetization had been fulfilled in the experiment.

The local spin magnetic moment for the Fe^{III} system obtained from XMCD quantitatively agrees with the corresponding value 1.9 $\pm$ 0.2 μ_{Bohr} of the Mn^{III} ions in the $\mathbf{[Mn^{III}_6Cr^{III}]^{3+}}$ SMM and with the corresponding values obtained from the SPES measurements analysis. However, only the local orbital magnetic moment for the Fe^{III} ions obtained from the XMCD case disappeared as expected for the Fe^{III} free ion case (L = 0, ^{6}S) or was thus completely quenched (0.01) by the very high magnetic field in contrast to the SPES measurement at room temperature without the magnetic field (0.56) and also to the results from the Mn-SMM (0.6 and 0.3). This is obviously a further hint that the Fe-system is not a SMM, like the Mn one. The sign of the spin and orbital local magnetic moments is the same for the Fe system as for the Mn SMM system.

Although the spin magnetic moment determined by the sum rule approaches from both XMCD and SPES data agree to a reasonable extent, the results are below the effective magnetic moments of the $\mathbf{[Fe^{III}_6Cr^{III}]^{3+}}$ ions shown in Figure 5b, which would correspond to a local spin moment of Fe to be 2.5 μ_{Bohr}. The observed discrepancy might also in part be attributed to the simplicity of the sum rule approach and the approximations employed in the derivation of the spin and orbital sum rules. See [47–54] for a more detailed discussion of their physical limitations. While the use of correction factors for spin sum rule results obtained from 3d systems [53] may represent an improvement, the quantitative applicability of this approach for molecular systems like $[Fe_6Cr]^{3+}$ might not be generally assumed without a more detailed theoretical investigation.

At the Cr $L_{2,3}$ edge at photon energies around 580 eV, an XMCD asymmetry of opposite sign compared to the Fe $L_{2,3}$ edge has been measured. Since a separation of the L_2 and L_3 contributions in the sum rule application could not be performed and electron spin polarizations have not been measured there, an analysis of Cr local spin and orbital magnetic moments could not be performed.

5. Summary and Conclusions

Comparative measurements using XMCD (4 K, 6.9 T) and spin-resolved electron spectroscopy (at room temperature, without external field) at the Fe L edge were performed on $\mathbf{[Fe^{III}_6Cr^{III}]}(ClO_4)_3$ thin films deposited on solid substrates. A simple sum rule evaluation was performed to enable a comparison of the two experimental methods, despite the known restrictions concerning the applicability to 3d systems. The absolute value of the local spin magnetic moment obtained from both methods agrees within the experimental errors. In cross-comparison with the recently studied $\mathbf{[Mn^{III}_6Cr^{III}]^{3+}}$ SMM, the spin polarization found for the Fe system were higher and showed the same absolute values as for the XMCD asymmetry. The local orbital Fe-magnetic moment has been completely quenched by the high magnetic field for the low temperature in the XMCD study, unlike the Mn SMM case.

Acknowledgments: Special thanks go to the Helmholtz-Zentrum Berlin (BESSY II) and the Paul Scherrer Institute Villigen (SLS), as well as their beamline staff for the continuous support throughout the numerous beam times. Karsten Kuepper acknowledges financial support by the collaborative research centre (SFB) 569 funded by the Deutsche Forschungsgemeinschaft (DFG). This work was supported by the Deutsche Forschungsgemeinschaft (DFG) within Research Unit 945.

Author Contributions: Radiation sensitivity and electron spin polarization measurements were performed by the group of Institution (1) using their own apparatus. The chemical synthesis and characterization of the molecules was completed by the group of Institution (2), and XMCD relates to Institutions (3 and 4).

Conflicts of Interest: The authors declare no conflict of interest.

References

1. Helmstedt, A.; Dohmeier, N.; Müller, N.; Gryzia, A.; Brechling, A.; Heinzmann, U.; Hoeke, V.; Krickemeyer, E.; Glaser, T.; Leicht, P.; *et al*. Probing the magnetic moments of $[Mn^{III}{}_6Cr^{III}]^{3+}$ single-molecule magnets—A cross comparison of XMCD and spin-resolved electron spectroscopy. *J. Electron Spectrosc. Relat. Phenom.* **2015**, *198*, 12–19. [CrossRef]
2. Wood, R. Future hard disk drive systems. *J. Magn. Magn. Mater.* **2009**, *321*, 555–561. [CrossRef]
3. Wood, R. The feasibility of magnetic recording at 1 Terabit per square inch. *IEEE Trans. Magn.* **2000**, *36*, 36. [CrossRef]
4. Stefanita, C.G. From bulk to nano. In *The Many Sides of Magnetism*; Springer Verlag: Berlin, Heidelberg, Germany, 2008; p. 131.
5. Charap, S.H.; Lu, P.L.; He, Y. Thermal Stability of Recorded Information at High Densities. *IEEE Trans. Magn.* **1997**, *33*, 978. [CrossRef]
6. Shiroishi, Y.; Fukuda, K.; Tagawa, I.; Iwasaki, H.; Takenoiri, S.; Tanaka, H.; Mutoh, H.; Yoshikawa, N. Future Options for HDD Storage. *IEEE Trans. Magn.* **2009**, *45*, 3816. [CrossRef]
7. Nickel, J.; Gibson, G. Beyond magnetic storage: Atoms and molecules. In *Magnetic Storage Systems beyond 2000*; Hadjipanayis, G.C., Ed.; Kluwer Academic Publishers: Dordrecht, The Netherlands, 2001; p. 599.
8. Hush, N.S. An overview of the first half-century of molecular electronics. *Ann. N. Y. Acad. Sci.* **2003**, *1006*, 1–20. [CrossRef] [PubMed]
9. Tsutsui, M.; Taniguchi, M. Single Molecule Electronics and Devices. *Sensors* **2012**, *12*, 7259–7298. [CrossRef] [PubMed]
10. Renaud, N.; Hliwa, M.; Joachim, C. Single molecule logical devices. In *Unimolecular and Supramolecular Electronics II - Chemistry and Physics Meet at Metal-Molecule Interfaces*; Metzger, R.M., Ed.; Springer Verlag: Berlin, Germany; Heidelberg, Germany, 2012; p. 217.
11. Christou, G.; Gatteschi, D.; Hendickson, D.; Sessoli, R. Single-molecule magnets. *MRS Bull.* **2000**, *25*, 66–71. [CrossRef]
12. Gatteschi, D.; Sessoli, R. Quantum Tunneling of Magnetization and Related Phenomena in Molecular Materials. *Angew. Chem. Int. Ed.* **2003**, *42*, 268–297. [CrossRef] [PubMed]
13. Gatteschi, D.; Sessoli, R.; Villain, J. *Molecular Nanomagnets*; Oxford University Press: Oxford, UK, 2006.
14. Tejada, J.; Chudnovsky, E.M.; del Barco, E.; Hernandez, J.M.; Spiller, T.P. Magnetic qubits as hardware for quantum computers. *Nanotechnology* **2001**, *12*, 181–186. [CrossRef]
15. Awschalom, D.D.; DiVincenzo, D.P.; Smyth, J.F. Macroscopic Quantum Effects in Nanometer-Scale Magnets. *Science* **1992**, *258*, 414. [CrossRef] [PubMed]
16. Leuenberger, M.N.; Loss, D. Quantum computing in molecular magnets. *Nature* **2001**, *410*, 789. [CrossRef] [PubMed]
17. Bogani, L.; Wernsdorfer, W. Molecular spintronics using single-molecule magnetsle. *Nat. Mater.* **2008**, *7*, 179. [CrossRef] [PubMed]
18. Mannini, M.; Pineider, F.; Danieli, C.; Totti, F.; Sorace, L.; Sainctavit, P.; Arrio, M.A.; Otero, E.; Joly, L.; Cezar, J.C.; *et al*. Quantum tunneling of the magnetization in a monolayer of oriented single-molecule magnets. *Nature* **2010**, *468*, 417. [CrossRef] [PubMed]
19. Rogez, G.; Donnio, B.; Terazzi, E.; Gallani, J.L.; Kappler, J.P.; Bucher, J.P.; Drillon, M. The Quest for Nanoscale Magnets: The example of [Mn12] Single Molecule Magnets. *Adv. Mater.* **2009**, *21*, 4323–4333. [CrossRef] [PubMed]
20. Winpenny, R.E.P. Serendipitous assembly of polynuclear cage compounds. *Dalton Trans.* **2002**, 1–10. [CrossRef]
21. Lis, T. Preparation, structure and magnetic properties of a dodecanuclear mixed-valence manganese carboxylate. *Acta Cryst.* **1980**, *B36*, 2042–2046. [CrossRef]
22. Sessoli, R.; Tasi, H.-L.; Schake, A.R.; Wang, S.; Vincent, J.B.; Folting, K.; Gatteschi, D.; Christou, G.; Hendrickson, D.N. High-Spin Molecules: $[Mn_{12}O_{12}(O_2CR)_{16}(H_2O)_4]$. *J. Am. Chem. Soc.* **1993**, *115*, 1804–1816. [CrossRef]
23. Bagai, R.; Christou, G. The Drosophila of single-molecule magnetism: $[Mn_{12}O_{12}(O_2CR)_{16}(H_2O)_4]$. *Chem. Soc. Rev.* **2009**, *38*, 1011–1026. [CrossRef] [PubMed]

24. Glaser, T.; Heidemeier, M.; Weyhermüller, T.; Hoffmann, R.D.; Rupp, H.; Müller, P. Property-oriented rational design of single-molecule magnets: A C_3-Symmetric Mn_6Cr complex based on three molecular building blocks with a spin ground state of $S_t = 21/2$. *Angew. Chem. Int. Ed.* **2006**, *45*, 6033–6037. [CrossRef] [PubMed]
25. Glaser, T. Rational design of single-molecule magnets: A supramolecular approach. *Chem. Commun.* **2011**, *47*, 116–130. [CrossRef] [PubMed]
26. Hoeke, V.; Heidemeier, M.; Krickemeyer, E.; Stammler, A.; Bögge, H.; Schnack, J.; Postnikov, A.; Glaser, T. Environmental influence on the single-molecule magnet behavior of $\mathbf{[Mn^{III}_6Cr^{III}]^{3+}}$: Molecular symmetry *versus* solid-state effects. *Inorg. Chem.* **2012**, *51*, 10929–10954. [CrossRef] [PubMed]
27. Glaser, T.; Heidemeier, M.; Krickemeyer, E.; Bögge, H.; Stammler, A.; Fröhlich, R.; Bill, E.; Schnack, J. Exchange interactions and zero-field splittings in C_3-Symmetric $Mn^{III}_6Fe^{III}$: Using molecular recognition for the construction of a series of high spin complexes based on the triplesalen ligand. *Inorg. Chem.* **2009**, *48*, 607–620. [CrossRef] [PubMed]
28. Von Richthofen, C.G.; Stammler, A.; Bögge, H.; de Groot, M.W.; Long, J.R.; Glaser, T. Synthesis, Structure, and Magnetic Characterization of a C-3-Symmetric (Mn3CrIII-Cr-III Assembly: Molecular Recognition Between a Trinuclear Mn-III Triplesalen Complex and a fac-Triscyano Cr-III Complex. *Inorg. Chem.* **2009**, *48*, 10165–10176. [CrossRef] [PubMed]
29. Krickemeyer, E.; Hoeke, V.; Stammler, A.; Bögge, H.; Schnack, J.; Glaser, T. Synthesis and characterization of the heptanuclear $\mathbf{[Mn^{III}_6Co^{III}]^{3+}}$ triplesalen complex: Evidence for exchange pathways involving low-spin Co^{III}. *Z. Naturforsch.* **2010**, *65*, 295–303. [CrossRef]
30. Hoeke, V.; Gieb, K.; Müller, P.; Ungur, L.; Chibotaru, L.F.; Heidemeier, M.; Krickemeyer, E.; Stammler, A.; Bögge, H.; Schröder, C.; *et al*. Hysteresis in the ground and excited spin state up to 10 T of a $\mathbf{[Mn^{III}_6Mn^{III}]^{3+}}$ triplesalen single-molecule magnet. *Chem. Sci.* **2012**, *3*, 2868–2882. [CrossRef]
31. Hoeke, V.; Heidemeier, M.; Krickemeyer, E.; Stammler, A.; Bögge, H.; Schnack, J.; Glaser, T. Structural influences on the exchange coupling and zero-field splitting in the single-molecule magnet $[Mn^{III}_6Mn^{III}]^{3+}$. *Dalton Trans.* **2012**, 12942. [CrossRef] [PubMed]
32. Hoeke, V.; Krickemeyer, E.; Heidemeier, M.; Theil, H.; Stammler, A.; Bögge, H.; Weyhermüller, T.; Schnack, J.; Glaser, T. A Comprehensive Study on Triplesalen-Based $\mathbf{[Mn^{III}_6Fe^{III}]^{3+}}$ and $\mathbf{[Mn^{III}_6Fe^{II}]^{2+}}$ Complexes: Redox-Induced Variation of Molecular Magnetic Properties. *Eur. J. Inorg. Chem.* **2013**, 4398–4409. [CrossRef]
33. Hoeke, V.; Stammler, A.; Bögge, H.; Schnack, J.; Glaser, T. Strong and anisotropic superexchange in the single-molecule magnet (SMM) $\mathbf{[Mn^{III}_6Os^{III}]^{3+}}$: Promoting SMM behavior through 3d-5d transition metal substitution. *Inorg. Chem.* **2014**, *53*, 257–268. [CrossRef] [PubMed]
34. Mukherjee, C.; Hoeke, V.; Stammler, A.; Bögge, H.; Schnack, J.; Glaser, T. Switching from antiferromagnetic to ferromagnetic coupling in Heptanuclear $\mathbf{[M^t_6M^c]^{n+}}$ complexes by going from an achiral to a chiral triplesalen ligand. *Dalton Trans.* **2014**, *43*, 9690–9703. [CrossRef] [PubMed]
35. Glaser, T.; Hoeke, V.; Gieb, K.; Schnack, J.; Schröder, C.; Müller, P. Quantum tunneling of the magnetization in $\mathbf{[Mn^{III}_6M]^{3+}}$ (M = Cr^{III}, Mn^{III}) SMMs: Impact of molecular and crystal symmetry. *Coord. Chem. Rev.* **2015**, *289–290*, 261–278. [CrossRef]
36. Helmstedt, A.; Sacher, M.D.; Gryzia, A.; Harder, A.; Brechling, A.; Müller, N.; Heinzmann, U.; Hoeke, V.; Krickemeyer, E.; Glaser, T.; *et al*. Exposure of $[MnIII_6CrIII]^{3+}$ single-molecule-magnets to soft X-rays: The effect of the counterions on radiation stability. *J. Electron Spectrosc. Relat. Phenom.* **2012**, *184*, 583–588. [CrossRef]
37. Helmstedt, A.; Müller, N.; Gryzia, A.; Dohmeier, N.; Brechling, A.; Sacher, M.D.; Heinzmann, U.; Hoeke, V.; Krickemeyer, E.; Glaser, T.; *et al*. Spin-resolved photoelectron spectroscopy of $[Mn^{III}_6Cr^{III}]^{3+}$ single-molecule-magnets and of manganese compounds as reference layers. *J. Phys. Condens. Matter* **2011**, *23*, 266001. [CrossRef] [PubMed]
38. Gryzia, A.; Predatsch, H.; Brechling, A.; Hoeke, V.; Krickemeyer, E.; Derks, C.; Neumann, M.; Glaser, T.; Heinzmann, U. Preparation of monolayers of $[Mn_6Cr]^{3+}$-single-molecule-magnets on HOPG-, mica- and silicon surfaces and characterization by means of nc-AFM. *Nanoscale Res. Lett.* **2011**, *6*, 486. [CrossRef] [PubMed]
39. Gryzia, A.; Volkmann, T.; Brechling, A.; Hoeke, V.; Schneider, L.; Kuepper, K.; Glaser, T.; Heinzmann, U. Crystallographic order and decomposition of $[Mn^{III}_6Cr^{III}]^{3+}$ single-molecule magnets deposited in submonolayers and monolayers on HOPG studied by means of molecular resolved atomic force microscopy (AFM) and kelvin probe force microscopy in UHV. *Nanoscale Res. Lett.* **2014**, *9*, 60. [CrossRef] [PubMed]

40. Wende, H.; Antoniak, C. X-ray magnetic dichroism. In *Magnetism and Synchrotron Radiation*; Beaurepaire, E., Bulou, H., Scheurer, F., Kappler, J.P., Eds.; Springer Proceedings in Physics; Springer Verlag: Berlin, Germany; Heidelberg, Germany, 2010; p. 145.
41. Sessoli, R.; Mannini, M.; Pineider, F.; Cornia, A.; Sainctavit, P. XAS and XMCD of single molecule magnets. In *Magnetism and Synchrotron Radiation*; Beaurepaire, E., Bulou, H., Scheurer, F., Kappler, J.P., Eds.; Springer Proceedings in Physics; Springer Verlag: Berlin, Germany; Heidelberg, Germany, 2010; p. 279.
42. Nakamura, T.; Suzuki, M. Recent Progress of the X-ray Magnetic Circular Dichroism Technique for Element-Specific Magnetic Analysis. *J. Phys. Soc. Jpn.* **2013**, *82*, 021006. [CrossRef]
43. Thole, B.T.; Carra, P.; Sette, F.; van der Laan, G. X-ray circular dichroism as a probe of orbital magnetization. *Phys. Rev. Lett.* **1992**, *68*, 1943. [CrossRef] [PubMed]
44. Carra, P.; Thole, B.T.; Altarelli, M.; Wang, X. X-ray circular dichroism and local magnetic fields. *Phys. Rev. Lett.* **1993**, *70*, 694. [CrossRef] [PubMed]
45. Scherz, A. Spin-Dependent X-ray Absorption Spectroscopy of 3D Transition Metals: Systematics and Applications. PhD Thesis, Freien Universität Berlin, Berlin, Germany, 2003.
46. Chen, C.T.; Idzerda, Y.U.; Lin, H.J.; Smith, N.V.; Meigs, G.; Chaban, E.; Ho, G.H.; Pellegrin, E.; Sette, F. Experimental Confirmation of the X-ray Magnetic Circular Dichroism Sum Rules for Iron and Cobalt. *Phys. Rev. Lett.* **1995**, *75*, 152. [CrossRef] [PubMed]
47. Wu, R.; Wang, D.; Freeman, A.J. First principles investigation of the validity and range of applicability of the x-ray magnetic circular dichroism, sum rule. *Phys. Rev. Lett.* **1993**, *71*, 3581. [CrossRef] [PubMed]
48. Wu, R.; Freeman, A.J. Limitation of the Magnetic-Circular-Dichroism Spin Sum Rule for Transition Metals and Importance of the Magnetic Dipole Term. *Phys. Rev. Lett.* **1994**, *73*, 1994. [CrossRef] [PubMed]
49. Schütz, G.; Fischer, P.; Attenkofer, K.; Knülle, M.; Ahlers, D.; Stähler, S.; Detlefs, C.; Ebert, H.; de Groot, F.M.F. X-ray magnetic circular dichroism in the near and extended absorption edge structure. *J. Appl. Phys.* **1994**, *76*, 6453. [CrossRef]
50. Van der Laan, G. Sum rule practice. *J. Synchrotron Rad.* **1999**, *6*, 694–695. [CrossRef] [PubMed]
51. Nesvizhskii, A.I.; Ankudinov, A.L.; Rehr, J.J. Normalization and convergence of X-ray absorption sum rules. *Phys. Rev. B* **2001**, *63*, 094412. [CrossRef]
52. Teramura, Y.; Tanaka, A.; Jo, T. Effect of Coulomb Interaction on the X-ray Magnetic Circular Dichroism Spin Sum Rule in 3d Transition Elements. *J. Phys. Soc. Jap.* **1996**, *65*, 1053–1055. [CrossRef]
53. Piamonteze, C.; Miedema, P.; de Groot, F.M.F. Accuracy of the spin sum rule in XMCD for the transition-metal L edges from manganese to copper. *Phys. Rev. B* **2009**, *80*, 184410. [CrossRef]
54. Kuepper, K.; Raekers, M.; Taubitz, C.; Uhlarz, M.; Piamonteze, C.; de Groot, F.M.F.; Arenholz, E.; Galakhov, V.R.; Mukovskii, Y.M.; Neumann, M. The X-ray magnetic circular dichroism spin sum rule for $3d^4$ systems: Mn^{3+} ions in colossal magnetoresistance manganites. *J. Phys. Condens. Matter* **2012**, *24*, 435602. [CrossRef] [PubMed]
55. Müller, N.; Lischke, T.; Weiss, M.R.; Heinzmann, U. Spin resolved photoelectron spectroscopy from paramagnetic Gd at the 4d -> 4f resonance using circularly-polarized radiation, a cross-comparison with MCD. *J. Electron Spectrosc. Relat. Phenom.* **2001**, *114–116*, 777–782. [CrossRef]
56. Heinzmann, U. Photoemission and absorption spectroscopy of solids and interfaces with synchrotron radiation. In *Proceedings of the International School of Physics "Enrico Fermi"*; Campagna, M., Rosei, R., Eds.; North-Holland Publishing Company: Amsterdam, The Netherland, 1990; p. 469.
57. Müller, N.; David, R.; Snell, G.; Kuntze, R.; Drescher, M.; Böwering, N.; Stoppmanns, P.; Yu, S.W.; Heinzmann, U.; Viefhaus, J.; *et al*. Spin-resolved Auger electron spectroscopy after photoexcitation with circularly polarized radiation from the BESSY crossed undulator. *J. Electron Spectrosc. Relat. Phenom.* **1995**, *72*, 187–193. [CrossRef]
58. Cherepkov, N.A.; Kuznetsov, V.V. Optical activity of polarized atoms. *J. Phys. B: At. Mol. Opt. Phys.* **1989**, *22*, L405–L409. [CrossRef]
59. Heinzmann, U.; Dil, J.H. Spin orbit induced photoelectron spin polarization in angle resolved photoemission from both atomic and condensed matter targets. *J. Phys. Condens. Matter* **2012**, *24*, 173001. [CrossRef] [PubMed]
60. Van der Laan, G.; Thole, B.T. Spin polarization and magnetic dichroism in photoemission from core and valence states in localized magnetic systems. IV. Core-hole polarization in resonant photoemission. *Phys. Rev. B* **1995**, *52*, 15355. [CrossRef]

61. Sheldrick, G.M. A short history of SHELX. *Acta Crystallogr.* **2008**, *A64*, 112–122. [CrossRef] [PubMed]
62. Sluis, P.V.D.; Spek, A.L. BYPASS: An effective method for the refinement of crystal structures containing disordered solvent regions. *Acta Crystallogr.* **1990**, *A46*, 194–201. [CrossRef]
63. The Cambridge Crystallographic Data Centre. Available online: http://www.ccdc.cam.ac.uk/data_request/cif (accessed on 20 August 2015).
64. Mukherjee, C.; Stammler, A.; Bögge, H.; Glaser, T. Do trinuclear triplesalen complexes exhibit cooperative effects?—Synthesis, characterization, and enantioselective catalytic sulfoxidation by chiral trinuclear Fe^{III} triplesalen complexes. *Chem. Eur. J.* **2010**, *16*, 10137–10149. [CrossRef] [PubMed]
65. Glaser, T. Exchange Coupling Mediated by Extended Phloroglucinol Ligands: Spin-Polarization *vs.* Heteroradialene-Formation. *Coord. Chem. Rev.* **2013**, *257*, 140–152. [CrossRef]
66. Feldscher, B.; Stammler, A.; Bögge, H.; Glaser, T. Aromatic *vs.* heteroradialene character in extended phloroglucinol and thiophloroglucinol ligands and their trinuclear nickel(ii) complexes. *Chem. Asian J.* **2014**, *9*, 2205–2218. [CrossRef] [PubMed]
67. Godehusen, K.; (BESSY-II, Helmholtz-Zentrum Berlin, Germany). UE52-SGM beamline technical Documentation, personal communication, 2009.
68. Mahler, W.; (FHI der MPG, BESSY-II, Helmholtz-Zentrum Berlin, Germany). UE56/2-PGM-2 beamline technical documentation, personal communication, 2013.
69. Sawhney, K.J.S.; Senf, F.; Scheer, M.; Schäfers, F.; Bahrdt, J.; Gaupp, A.; Gudat, W. A novel undulator-based PGM Beamline for circularly polarized synchrotron radiation at BESSY II. *Nucl. Instrum. Meth. A* **1997**, *390*, 395–402. [CrossRef]
70. Gray, L.G.; Hart, M.W.; Dunning, F.B.; Walters, G.K. Simple, compact, medium-energy Mott polarization analyzer. *Rev. Sci. Instrum.* **1984**, *55*, 88–91. [CrossRef]
71. Müller, N.; Khalil, T.; Pohl, M.; Uphues, T.; Polcik, M.; Rader, O.; Heigl, F.; Starke, K.; Fritzsche, S.; Kabachnik, N.M.; *et al*. Interference of spin states in resonant photoemission induced by circularly polarized light from magnetized Gd. *Phys. Rev. B* **2006**, *74*, 161401R. [CrossRef]
72. David, R.; Stoppmanns, P.; Yu, S.W.; Kuntze, R.; Müller, N.; Heinzmann, U. Circularly polarized undulator radiation from the new crossed double-undulator beamline at BESSY and its first use for spin resolved Auger electron emission spectroscopy. *Nucl. Instrum. Meth. A* **1994**, *343*, 650–654. [CrossRef]
73. Stepanow, S.; Mugarza, A.; Ceballos, G.; Moras, P.; Cezar, J.C.; Carbone, C.; Gambardella, P. Giant spin and orbital moment anisotropies of a Cu-phthalocyanine monolayer. *Phys. Rev. B* **2010**, *82*, 014405. [CrossRef]
74. Stöhr, J.; König, H. Determination of spin- and orbital-moment anisotropies in transition metals by angle-dependent X-ray magnetic circular dichroism. *Phys. Rev. Lett.* **1995**, *75*, 3748–3751. [CrossRef] [PubMed]